A Dissection of Oligomerization by the TRIM28 Tripartite Motif and the Interaction with Members of the Krab-ZFP Family

Yunyuan Sun [1], Jeremy R. Keown [1], Moyra M. Black [1], Charlène Raclot [2], Nicholas Demarais [1], Didier Trono [2], Priscilla Turelli [2] and David C. Goldstone [1]

*1 - **School of Biological Sciences,** University of Auckland, Auckland, New Zealand*
*2 - **EPFL,** Lausanne, Switzerland*

***Correspondence to David C. Goldstone:** d.goldstone@auckland.ac.nz*
https://doi.org/10.1016/j.jmb.2019.05.002
Edited by Dylan Taatjes

Abstract

TRIM28 (also known as KAP1 or TIF1β) is the universal co-repressor of the Krüppel-associated box-containing zinc finger proteins (Krab-ZFPs), the largest family of transcription factors in mammals. During early embryogenesis, TRIM28 mediates the transcriptional silencing of many endogenous retroviral elements and genomic imprinted sites. Silencing is initiated by the recruitment of TRIM28 to a target locus by members of the Krab-ZFP. Subsequently, TRIM28 functions as a scaffold protein to recruit chromatin modifying effectors featuring SETDB1, HP1 and the NuRD complex. Although many protein partners involved in silencing have been identified, the molecular basis of the protein interactions that mediate silencing remains largely unclear. In the present study, we identified the first Bbox domain (T28_B1 135–203) as a molecular interface responsible for the formation of higher-order oligomers of TRIM28. The structure of this domain reveals a new interface on the surface of the Bbox domain. Mutants disrupting the interface disrupt the formation of oligomers but have no observed effect on transcriptional silencing defining a single TRIM28 dimer as the functional unit for silencing. Using assembly-deficient mutants, we employed small-angle X-ray scattering and biophysical techniques to characterize binding to member of the Krab-ZFP family. This allows us to narrow and define the binding interface to the center of the coiled-coil region (residues 294–321) of TRIM28 and define mutants that abolish binding to the Krab-ZFP proteins.

Introduction

Endogenous retroviruses (ERVs) arise when a retrovirus infects the host's germ line and becomes inherited in a Mandelian manner. It is estimated that over 50 waves of endogenization have occurred in ancestral human lineages with ERVs now comprising approximately 8% of the human genome [1]. ERVs form a class of retrotransposons that can move around the host genome causing mutational insertions. To protect genome integrity, humans and other mammalian hosts undergo targeted silencing of ERVs during embryogenesis via TRIM28-mediated repression of transcription. The deletion of TRIM28 in mouse embryonic stem (ES) cells leads to substantial de-repression of a range of murine ERVs [2,3]. In addition to genome protection, the TRIM28/Krab-ZFP system also enables the host to domesticate the transcription potential of ERVs for regulating the expression of host genes and developing gene networks [1,4].

TRIM28 (or KAP1 or TIF1β) belongs to the *tri*partite *m*otif (TRIM) protein family with over 70 members in the human genome [5]. The family shares a conserved N-terminal domain organization, termed the RBCC or tripartite motif, consisting of a RING domain, followed by one or two B-box domains and a coiled-coil region. The C-terminal domains of TRIM proteins are variable and have been used to classify the family into 11 subfamilies [6]. TRIM28 belongs to the TIF1 subfamily, along with TRIM24 and TRIM33, that share a C-terminal PHD/Bromo domain. The PHD/Bromo domain of TRIM24 and TRIM33 are both histone code readers [7,8]. In contrast, the PHD/Bromo of TRIM28 does not recognize histone tails but acts as an intramolecular E3 SUMO ligase [9,10]. Auto-SUMOylation in the PHD/Bromo domain is a major determinant of TRIM28's

repressive activity, as mutants lacking SUMOylation sites display an almost complete loss of repression [10,11].

To target a specific site, TRIM28 itself does not bind DNA, rather it acts as the universal co-repressor for the Krüppel-associated box-containing zinc finger proteins (Krab-ZFPs). The Krab-ZFPs are the largest family of transcription factors in mammals with over 350 members in humans and other mammals [12,13]. The expansion of Krab-ZFPs in mammalian genomes is thought to be due to a requirement to silence ERVs during bursts of viral endogenization [14,15]. Indeed many Krab-ZFPs recognize ERV loci [13,16,17]. The most thoroughly characterized system is the targeting of both endogenous and exogenous murine leukemia virus by ZFP809. ZFP809 recognizes the PBS^{Pro} primer binding site region of the integrated virus during early stages of embryo development, preventing transcription from the retroviral promoter, facilitating immunity against the integrated virus [18].

Members of the Krab-ZFP family contain discrete N- and C-terminal domains each with a specific function. An array of between 2 and 40 zinc-finger domains are located at the C-terminal end of the protein [12]. Each zinc-finger recognizes three consecutive nucleotides [19] mediating recognition of specific DNA sequences. The N-terminal Krab domain is reported to be intrinsically disordered and is responsible for recruiting TRIM28 [20–24]. The Krab domain can be further divided into two subdomains encoded by separate exons. The more conserved N-terminal Krab-A box (~42 amino acids) is necessary and sufficient for TRIM28 binding and repression [24–26]. The Krab-B box (~30 amino acids), although not required for repression, can potentiate Krab-A mediated repression in an unknown mechanism [24,27,28]. Some Krab-ZFPs lack the Krab-B box altogether [12]. Structural studies into Krab domains indicate that it is mostly intrinsically disordered and likely folds upon interaction with TRIM28 [29,30].

Following recruitment to the host chromatin, TRIM28 is auto-SUMOylated [9,11] and recruits the histone methyltransferase SETDB1, the histone deacetylase-containing NuRD complex, and heterochromatin protein 1 (HP1). Collectively, these proteins mediate the conversion of euchromatin to heterochromatin, thereby silencing transcription [31,32].

The coiled-coil domain of TRIM proteins forms an antiparallel dimer that separates the N-terminal RING and Bbox domains onto opposite ends of the approximately 170 Å coiled-coil [33,34]. It has been shown that many TRIM proteins further assemble into functionally important higher-order assemblies. The RING domains of TRIM23 and TRIM32 form homodimers to activate their E3 ubiquitin ligase activity [35,36]. The HIV restriction factor TRIM5α can trimerize via the Bbox 2 domain, facilitating the assembly of the protein into a hexagonal lattice on the retroviral capsid upon viral entry [37,38]. This assembly also brings the adjacent RING domains in close proximity to facilitate activity as an E3 ubiquitin ligase [38–40]. It has previously been reported that TRIM28 can form higher-order assemblies [41]; however, the detail and biological relevance of this has not been explored. In this study we identify the first Bbox domain (B1) of TRIM28 as the assembly interface for higher-order assembly. We have determined the structure of this domain and shown that B1 dimerization is not a requirement for Krab binding and auto-SUMOylation activity *in vitro*, and dimerization-null mutants were able to rescue the expression of an endogenous retroviral reporter in TRIM28 KD hESC cells. We have also shown that the Krab domain interacts with the central region of TRIM28 coiled-coil with a defined 2:1 stoichiometry and identified a single-point mutation in this region that abolishes the interaction with the Krab domain.

Results

TRIM28 assembles via its first Bbox domain

Previous investigations of TRIM28 self-association have reported assemblies ranging from a trimer to a hexamer [41], demonstrating that the protein undergoes higher-order assembly. However, these are at odds with the dimeric nature of the TRIM protein antiparallel coiled-coil. To better understand the molecular determinants of higher-order assembly for TRIM28, we purified a panel of TRIM28 truncation constructs spanning various domains (Fig. 1A) and used size exclusion chromatography coupled to multiangle laser light scattering (SEC-MALLS) analysis to assess the regions responsible for assembly.

Both the full-length protein T28_FL (residues 58–834 with the, N-terminal alanine-rich region removed) and the N-terminal tripartite motif T28_RBCCH (residues 58–597, RBCC including the HP1 binding region) eluted from the size-exclusion column as single asymmetric peaks with a long trailing edge, characteristic of a protein that self-assembles (Fig. 1B). The measured M_W (weight averaged molar mass) varied across the peak with the maximum M_W for T28_FL of 329 kDa for a sample injected at 70 μM. Both the peak position and observed M_W showed a strong concentration dependence with the M_W decreasing as the concentration for the injected sample was decreased from 70 to 18 μM. A similar result was also seen for T28_RBCCH. Analysis of the PHD/Bromodomain (T28_PB) showed no concentration dependence with the protein eluting as a single symmetric peak with a M_W of 23.3 kDa consistent with the predicted monomer mass of 23.2 kDa. From this, we conclude that the domain responsible for higher-order assembly is located within the N-terminal RBCC motif.

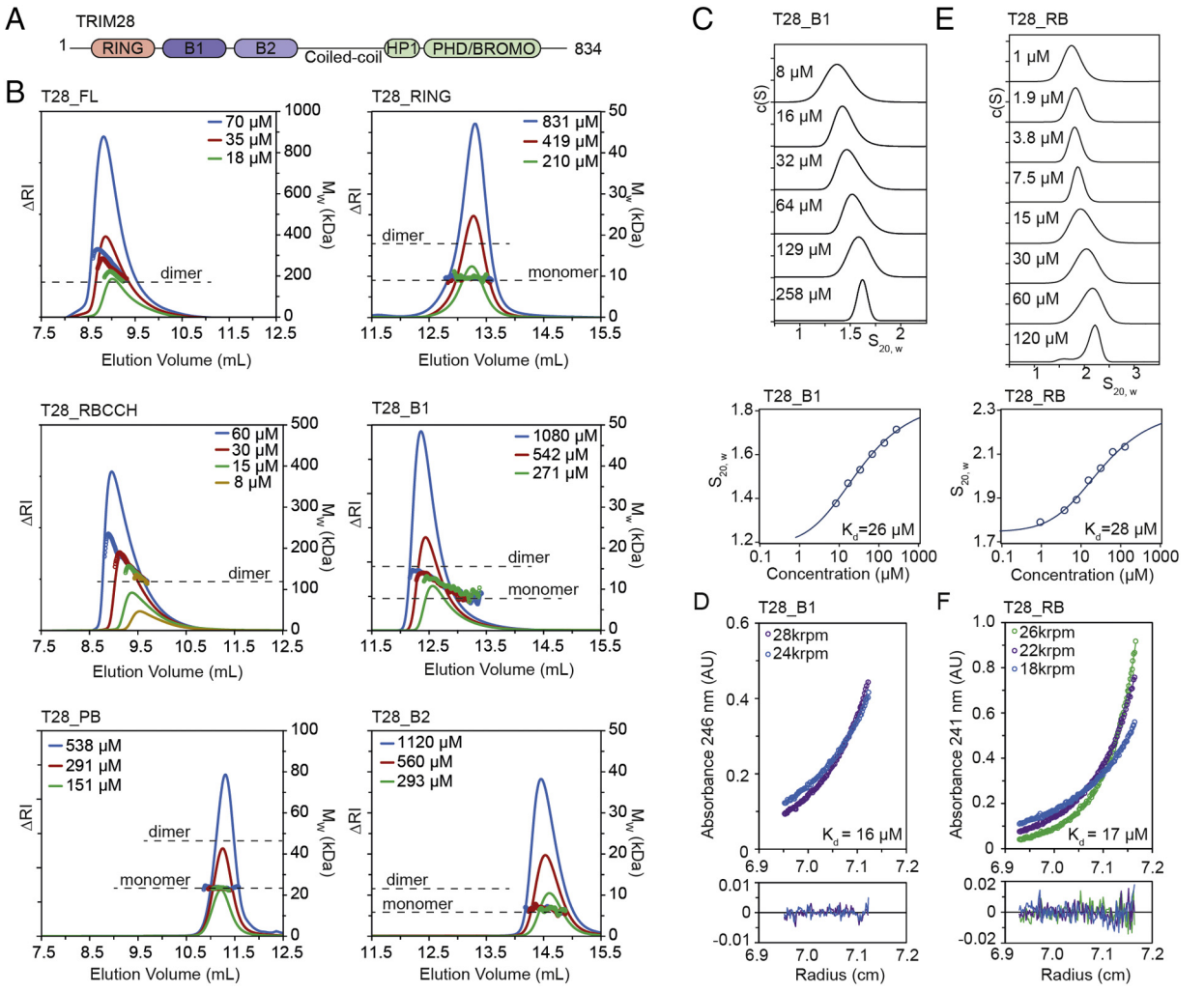

Fig. 1. TRIM28 Bbox 1 forms homodimer with low micromolar affinity. (A) Domain organization of TRIM28. (B) SEC-MALLS analysis of T28 FL, RBCCH (residues 58–597), PD, RING, B1 and B2 domains. Protein elution profile is shown as differential refractive indices (ΔRI) (solid lines). Circular markers represent the calculated M_W. Several loading concentrations were performed for each construct. (C and E) SV-AUC $c(S)$ analysis (upper) of TRIM28 B1 and RB at various protein concentrations. Isotherm analysis (lower) of TRIM28 B1 and RB fit to a monomer–dimer equilibrium model is shown. (D and F) Multispeed SE-AUC of TRIM28 B1 and RB. Data were fit into a monomer–dimer equilibrium model. A single representative starting concentration is shown in the upper panels. Lower panels show the residuals of the fits.

We subsequently examined the contribution of domains from within the tripartite motif. The RING domain (T28_RING) eluted as a single symmetric peak with a M_W that matched well to the monomer mass. The elution peaks of both Bbox domains (T28_B1 and T28_B2) were asymmetric with evidence of concentration dependence in both the peak retention volume and M_W, displaying concentration dependent self-association.

The structure of the T28_B2 domain (PDBid: 2YVR) has previously been determined by X-ray crystallography and forms a dimer within the crystal via the face of the central β-sheet. Alignment of this domain onto the Bbox-coiled-coil structure of the retroviral restriction factor TRIM5α (PDBid: 4TN3) shows that this interface would pack against the coiled-coil hairpin (Supplementary Fig. S1), suggesting that this assembly is an artifact of the crystallization. Consequently, we focussed our investigation on the first Bbox domain, T28_B1.

The TRIM28 B1 domain forms a homodimer

To further investigate assembly of T28_B1, we undertook sedimentation velocity (SV-AUC) and sedimentation equilibrium analytical ultracentrifuge (SE-AUC) experiments. SV-AUC experiments show a single peak with a concentration-dependent S-value ($S_{20,w}$ = 1.38 S to 1.71 S between 8 and 258 μM) (Fig. 1C). Fitting the $S_{20,w}$ isotherm to a

monomer–dimer equilibrium model, we estimate a K_d of 26 μM, with an $S_{20,w}$ of 1.23 for the monomer and an $S_{20,w}$ of 1.89 for the dimer. Multi-speed SE-AUC was undertaken to determine the stoichiometry and affinity of the self-assembly. Data were fit progressively with a monomer–dimer and monomer–trimer model using the program SEDPHAT. The best fit was obtained from a monomer–dimer equilibrium (Chi^2 = 0.345) with a dissociation constant (K_d) of 16 μM (Fig. 1D), in good agreement with the K_d determined from the S_w isotherm analysis.

Previously, it was observed that, despite being monomeric in solution, the RING domain from TRIM5α increases the strength of oligomerization of the Bbox2 domain alone [38]. To investigate the potential contribution of the RING domain to B1 dimerization, we performed SV- and SE-AUC on a construct comprising both the RING and B1 domain (T28_RB1 residues 58–203). The results were essentially identical to that of T28_B1 alone (SV-AUC K_d = 28 μM and SE-AUC K_d = 17 μM) (Fig. 1E, F). Therefore, the RING domain of TRIM28 does not contribute to B1 dimerization, suggesting that T28_B1 alone is responsible for the higher-order assembly of TRIM28.

Structure of B1 domain reveals dimer interface

To understand the molecular determinants of TRIM28 higher-order assembly, we determined the crystal structure of T28_B1. Crystallization trials resulted in long rod-like crystals in hanging drops equilibrated over 2.7 M ammonium sulfate at pH 6.0 after 3 days. Crystals were harvested into cryoprotectant containing 20% glycerol and flash frozen prior to data collection. Crystals belonged to the space group $P2_12_12_1$, and the structure was phased using single-wavelength anomalous dispersion based on the endogenous zinc atoms. The model was refined to a resolution of 1.6 Å (R_{work}/R_{free} of 18%/20.8%, respectively). Details of data collection, phasing, and model refinement are presented in Table 1.

Two copies of T28_B1 were present in the asymmetric unit. Well-defined electron density was obtained for residues spanning the entire Bbox domain, specifically, residues 151–196 in chain A and 154–196 in chain B. The N- and C-terminal regions could not be modeled, likely due to flexibility. The overall fold of the TRIM28 B1 resembles B1 and B2 domains from other members of the TRIM family. Each domain comprises a three-stranded anti-parallel β-sheet and a three-turn helix followed immediately by a short one-turn helix, in a β1–β2–α1–α2–β3 manner (Fig. 2A). Each Bbox contains two tetrahedral coordinated zinc atoms. The first zinc is coordinated by C154 and C157 on the N-terminal loop, C175 in the β2–α1 loop, and C178 in the N-terminus of α1. The second zinc binding site is formed by C167 in β1, C170 in the β1–2 loop, H182 in α1 and H191 in the α2–β3 loop.

Table 1. X-ray data collection and refinement statistics

Data collection	
Space group	$P2_12_12_1$
Cell dimensions	
a, *b*, *c* (Å)	33.0, 51.5, 72.9
α, *β*, *γ* (°)	90, 90, 90
Wavelength (Å)	0.9537
Resolution (Å)	42.0–1.6 (1.63–1.60)
No. of reflections	243,697 (11,629)
No. of unique	17,060 (817)
R_{merge}	0.267 (3.950)
R_{pim}	0.072 (1.075)
$I/\sigma I$	10.3 (0.97)
CC1/2	0.997 (0.391)
Completeness, %	100 (100)
Multiplicity	14.3 (14.2)
Anom multiplicity	7.7 (7.5)
Phasing	
FOM (SHELX)	0.606
Refinement	
Resolution (Å)	42.0–1.6
R_{work}/R_{free}	18.0/20.8
No. of atoms	746
Protein	698
Zinc	4
Solvent (water)	44
B-factors	
Wilson *B*	14.46
Average	27.85
Clash score	0
Ramachandran favored	100%
MolProbity score	1.00
Rmsd	
Bond lengths (Å)	0.007
Bond angles (°)	1.19

Values in parentheses are for the highest-resolution shell.

Our model revealed a dimer interface not previously observed in Bbox structures from other TRIM family members. The C-terminus of α1 from each monomer crosses together to form the dimer interface, which is stabilized by a hydrophobic core formed by each monomer's A181 and V185 in α1 (Fig. 2B). The dimer interface is further stabilized by the surrounding electrostatic interactions. A positively charged patch on the α1–α2 turn comprising R184 in α1 and K186, K189 in α2 packs against the negatively charged N-terminal loop and β1–2 loop. R184 in α1 from each monomer forms a salt-bridge with D159 in the N-terminal loop of the opposing monomer (Fig. 2B).

Structure-based mutagenesis disrupting higher-order assembly

To probe the T28_B1 dimer interface, we undertook site-directed mutagenesis of residues in the dimer interface. Three mutants were designed to disrupt the hydrophobic interaction (A181S, A181D, V185D), and three were designed to alter the charge

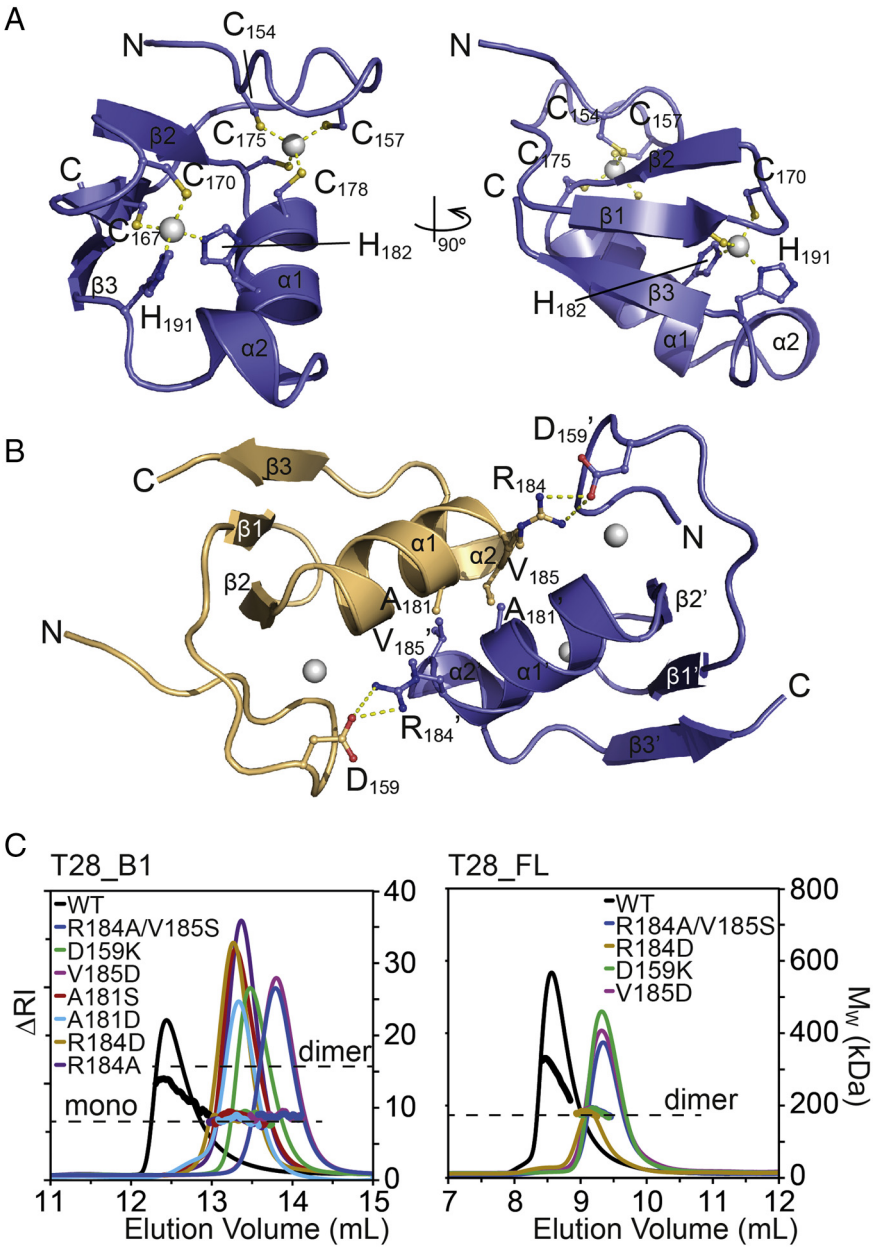

Fig. 2. Crystal structure of the murine TRIM28 B1 domain reveals a dimeric interface. (A) Cartoon representation of the murine TRIM28 B1 structure. Zinc atoms are shown as gray spheres and the coordinating residues as sticks. (B) Details of the B1 dimer interface with key residues comprising the interface shown as sticks. (C) SEC-MALLS analysis of the dimerinterface mutants in both T28_B1 domain (left) and T28_FL (right) compared to their WT counterparts. Single loading concentration is shown for each construct: B1 WT, 542 μM; B1_R184A/V185S, 631 μM; B1_D159K, 580 μM; B1_V184D, 671 μM; B1_A181S, 747 μM; B1_A181D, 516 μM; B1_R184D, 700 μM; B1_R184A, 757 μM; FL_WT, 70 μM; FL_ R184A/V185S, 85 μM; FL_R184D, 21 μM; FL_D159K, 51 μM; and FL_V185D 50 μM. The change in elution postion for V185D and R184A/V185S corresponds to a change in column used in the experiment and has no effect on the solution molecular weight.

on the salt-bridge (D159K, R184A, R184D), as well as one double mutant R184A/V185S. When incorporated into B1, all seven mutations severely disrupted dimerization of the T28_B1 domain compared to the wild type (Fig. 2C and Supplementary Fig. S4). Five mutations abolished dimerization: A181S, V185D, R184A, R184D and R184A/V185S, while D159K and A181S retained low levels of self-association (Supplementary Fig. S4). Four mutations R184D, D159K, V185D and R184A/V185S were then individually incorporated into the T28_FL protein, and their effect on assembly of the full-length protein was assessed.

All mutations abolished the higher-order assembly in T28_FL while retaining the dimer formed by the coiled-coil region (Supplementary Fig. S4). This demonstrates that the B1 domain of TRIM28 is responsible for the observed assembly of the full-length protein beyond a dimer.

Since auto-SUMOylation is a key determinant of TRIM28-mediated silencing [9,11], we next investigated the role of higher-order assembly in auto-SUMOylation. Both the RING domain and PHD/Bromo domain of TRIM28 have been shown to act as E3 SUMO ligases. PHD domain is an intramolecular SUMO ligase that targets the four SUMOylation sites found in the adjacent Bromodomain, a required step for TRIM28-mediated repression [9–11]. We carried out an *in vitro* auto-SUMOylation assay to assess the SUMOylation activity in the WT and the assembly-null variants. We observed a time-dependent appearance of SUMOylated species (mono-, di-, and tri-SUMOylated) for the full-length (FL, 58–834) WT protein during the 3-h incubation period (Fig. 3A). A similar level of SUMOylation is observed in the FL_R184D mutant. Surprisingly, we also observed the appearance of SUMOylated species (mono- and di-SUMOylated) for the T28_RBCCH construct (Fig. 3B), which lacks the PHD/Bromo domain but does contain two identified SUMOylation sites (K554 and K575) located in the predicted loop region upstream of the PHD domain [9,11]. This indicates that the RING domain can act as an E3 SUMO ligase for one or both of these sites. The level of SUMOylation in RBCCH is similar between the WT and the R184A variant. Therefore, higher-order assembly via T28_B1 dimerization is not required for TRIM28's auto-SUMOylation activity by either the RING domain or the PHD/Bromodomain.

To assess the effect of Bbox dimerization and higher-order assembly on transcriptional silencing, we undertook rescue assays in TRIM28 KD cells [16]. The four assembly-blocking mutations D159K, A181D, R184D and V185D were individually introduced into the human TRIM28 protein, and the mutants could rescue TRIM28-dependent repression of a reporter gene in KD cells (Fig. 3C). Based on these results, we conclude that disruption of TRIM28 oligomerization does not alter the transcription silencing phenotype. This therefore implies that a single copy of the TRIM28 dimer at the target locus is sufficient to mediate effective silencing.

TRIM28 RBCC forms a tight 2:1 complex with the Krab domain

Based on the requirement for only a single TRIM28 dimer at sites of silencing, we next sought to characterize the interaction between TRIM28 and members of the Krab-ZFP family. The presence of higher-order oligomers makes characterization of this interaction difficult; consequently, our assembly-blocking mutants are an ideal tool to characterize this interaction. We expressed and purified the Krab domain from three Krab-ZFP family members, ZFP809 (residues 1–74), Kid3 (14–84) and ZFP932 (5–76), as fusions to an N-terminal maltose binding protein (MBP)-tag. These Krab domains are well documented to interact with TRIM28 [4,18,42] and encompass the two major classes of Krab domains; ZFP809 and Kid3 belong to the Krab A + B class, while ZFP932 belongs to the Krab-A-only class. The MBP-tag acts as both a solubilisation tag aiding the expression and purification of the short Krab domain, and also increases the molecular mass of the protein aiding in the biophysical analysis.

To map the Krab binding site on TRIM28, we undertook pulldown assays on several TRIM28 truncation constructs. Our results show that the T28_FL, T28_RBCC and the T28_B2CC (201–597) readily bound to MBP-Krab (ZFP809), but not to the MBP-only negative control (Fig. 4A, B). All constructs lacking an intact coiled-coil region failed to bind, indicating that the coiled-coil forms the principal binding interface.

Using the assembly-blocking T28_RBCC_R184D, we next undertook SEC-MALLS analysis to investigate the stoichiometry of the TRIM28/Krab complex (Fig. 5A, Supplementary Fig. S5). T28_RBCC_R184D eluted from the column as a single peak at 11.5 mL with a calculated M_W of 82 kDa consistent with a dimer. All three MBP-Krab constructs, MBP-Krab-ZFP809, MBP-Krab-Kid3 and MBP-Krab-ZFP932, eluted at approximately 14.5 mL with a M_W of 52 kDa, accurately matching their respective theoretical masses of 52.1, 51.7, and 52.4 kDa. Next we loaded T28_RBCC_R184D/MBP-Krab-Kid3 at a 1:1 molar ratio, we observed the complete disappearance of the T28_RBCC_R184D peak at 11.5 mL, and the appearance of a peak with a retention volume of 11 mL corresponding to the T28-Krab complex. The MBP-Krab peak at 14.5 mL persisted, indicating that not all of the MBP-Krab-Kid3 was involved in binding. When we doubled the MBP-Krab-Kid3 concentration to a 1:2 molar ratio of T28_RBCC_R184D to MBP-Krab-Kid3, we saw a corresponding increase in the size of the MBP-Krab-Kid3 peak, but the complex peak at 11 mL remained essentially identical. Finally, a 2:1 molar ratio of T28_RBCC_R184D to MBP-Krab-Kid3 was loaded. The MBP-Krab-Kid3 peak disappeared, while the complex peak remained identical, indicating that all the MBP-Krab-Kid3 were involved in binding at this ratio. Similar results were observed with MBP-Krab-ZFP809 and MBP-Krab-ZFP932 (Supplementary Fig. S5). Light scattering analysis of the complex peak for each ratio showed an invariant M_W of 134 kDa, indicating that the complex formed is stable and monodisperse, with M_W perfectly matching the combined molar mass of 2 RBCC monomers (1 RBCC dimer) and 1 MBP-Krab. To corroborate this result, we also undertook native mass spectrometry on the

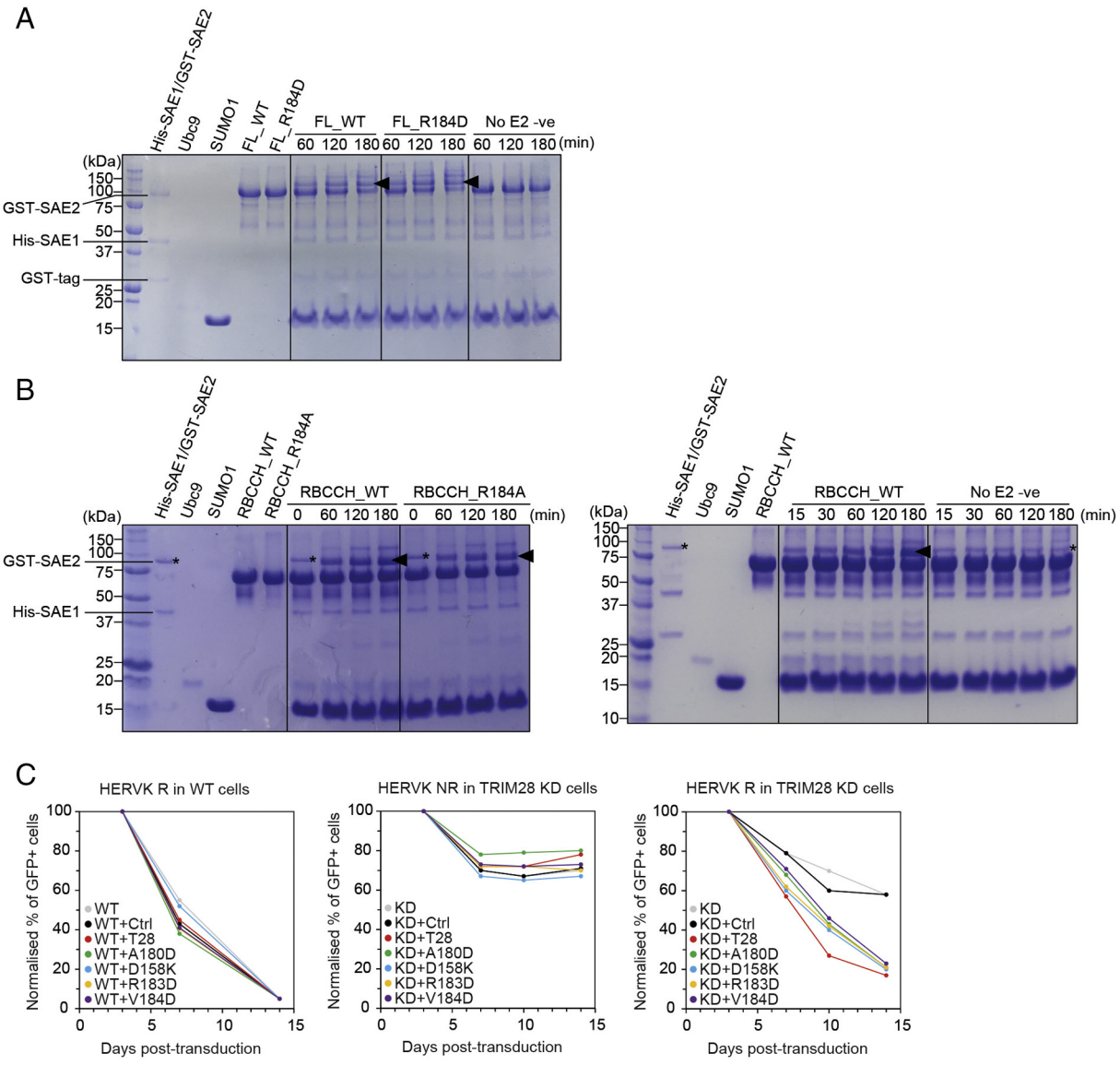

Fig. 3. B1 homodimer is not required for repression. (A, B) *In vitro* SUMOylation assay of T28_FL WT *versus* R184D and T28_RBCCH (residues 58–597) WT *versus* R184A mutant. Arrows mark the positions of mono-SUMOylated species. A negative control lacking the E2 enzyme is shown for comparison. (C) Cellular assay showing TRIM28 assembly-deficient variants can rescue reporter repression in TRIM28 KD cells. Lentiviral vectors expressing WT or mutant TRIM28 were transduced into TRIM28 KD (right and middle) and WT (positive control, left) hESC cells that possess a GFP reporter cassette silenced by an upstream TRIM28-bound HERVK repressed (HERVK R) sequence. A negative control with hESC cells containing an HERVK non-repressed sequence (HERVK NR), a variant that is not bound by TRIM28, was also performed. Reporter signal has been normalized to 3 days post-transduction and the average of duplicates is shown.

complex formed between T28_RBCC_R184D and MBP-Krab (Kid3 14–84). The protein sample was injected at a 1:1 molar ratio. The analysis revealed the presence of free MBP-Krab, as well as the 2:1 RBCC to MBP-Krab complex, but not a 2:2 complex (Supplementary Fig. S6). Taken together, our data demonstrate that a single Krab domain binds to a dimer of TRIM28, and this binding mode is shared across both the A + B and A-only classes.

The complete transition of the T28_RBCC to a stoichiometric complex with the Krab points to an extremely tight interaction. To further characterize this binding, we undertook Biacore SPR on T28_FL_R184D and T28_RBCC_R184D to examine their binding to immobilized Krab domains from ZFP809, Kid3, and ZFP932. The Krab domains were expressed with an N-terminal Avitag resulting in a monobiotinylated construct that was then immobilized onto the surface

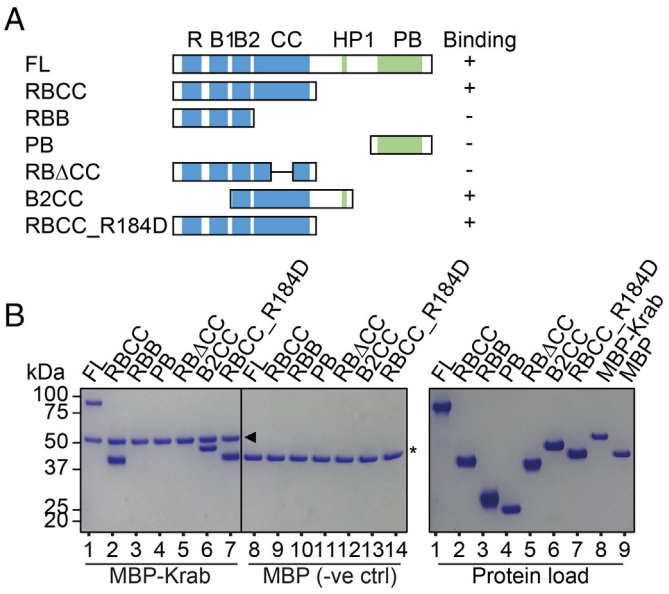

Fig. 4. Krab domain binds to the B2CC region of TRIM28. (A) Recombinant TRIM28 constructs used in MBP pulldown experiments with recombinant MBP-Krab fusion (ZFP809 residues 1–74) or MBP (negative control). (B) MBP pulldown assays visualized by Coomassie-stained SDS-PAGE analysis. (Left) Elution profile displaying various TRIM28 constructs and the RBCC_R184D variant bound to MBP-Krab but not to MBP. (Right) Purified recombinant proteins used in pulldown assays. Black arrow and asterisk mark the position of MBP-Krab and MBP, respectively.

of a biacore Sensor Chip CAP. T28_FL_R184D (400 nM) or T28_RBCC_R184D (206 nM) were injected over the chip surface for 120 s followed by a buffer wash for 600 s to allow dissociation. The dissociation constant K_d values determined between Krab domain and the TRIM28 FL were 11.8, 138.7 and 14.7 nM for ZFP809, Kid3 and ZFP932, respectively (Fig. 5B). Interestingly, K_d values determined between these Krab domains and RBCC were 2.29, 25.5 and 4.74 nM, respectively (Fig. 5C), approximately 3- to 5-fold stronger compared to the FL protein, suggesting that the presence of the C-terminal domains influences binding.

Krab domain interacts with the central region of TRIM28 coiled-coil

The binding experiments show a strong interaction between the Krab domain and TRIM28 with a clear stoichiometry of one TRIM28 dimer binding one Krab domain. This stoichiometry fits a model where a single Krab-ZFP is bound to DNA at a specific site and recruits a single TRIM28 dimer. However, based on the internal symmetry of the coiled-coil domain, we would expect two equivalent binding sites in the TRIM28 dimer. This suggests that Krab binding results in the occlusion of the equivalent site in the

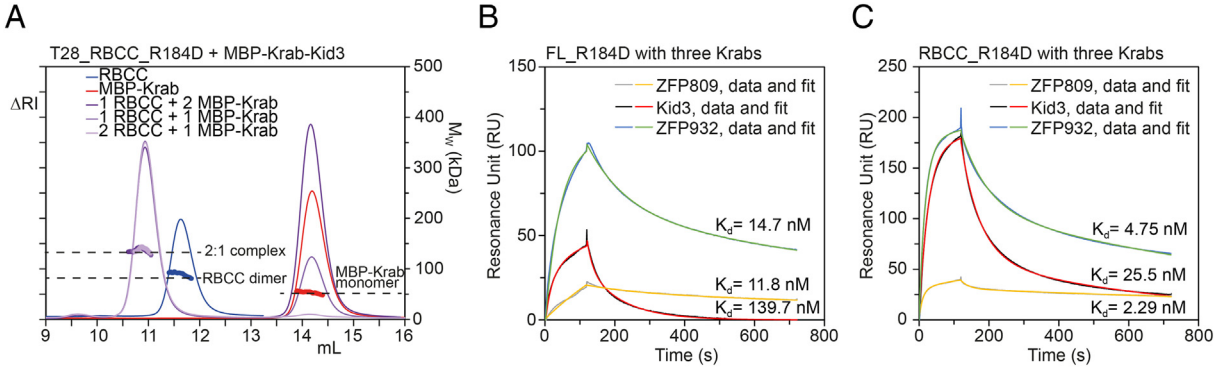

Fig. 5. Krab binds to the center of TRIM28 coiled-coil at a 1 Krab to 1 TRIM28 dimer ratio. (A) SEC-MALLS analysis of the $RBCC_{58–418}$_R184D/MBP-Krab protein complex for the Krab domain of Kid3. MBP-Krab is loaded at various molar ratios (1:1, 1:2 and 2:1) to TRIM28 RBCC. Protein elution profile is shown by differential refractive indices (solid lines), and their M_W is represented by open circles. Biacore SPR kinetics analysis of TRIM28 FL_R184D (B) and RBCC_R184D (C) with the Krab domains of ZFP809, Kid3 and ZFP932. Monobiotinylated Krab domains are immobilized onto the surface of a CAP sensor chip, and TRIM28 FL_R184D or RBCC_R184D was injected onto the chip surface. Sensograms have been fitted using BiacoreX100 Evaluation Software version 2.0.1.

other half of the protein. Since a construct spanning the B2 domain and coiled-coil of TRIM28 is sufficient to bind Krab, we hypothesized that the Krab domain binds to the central region of TRIM28 coiled-coil near the 2-fold symmetry axis, such that the binding to one site excludes the binding to the second equivalent site on the TRIM28 coiled-coil. This is supported by the lack of binding to the T28_RBΔCC construct lacking the central region of the coiled-coil.

To gain structural insights, we performed size exclusion chromatography coupled to small-angle x-ray scattering (SEC-SAXS) on T28_RBCC_R184D and the T28_RBCC_R184D/MBP-Krab (ZFP809 1–74) complex. The stable nature of RBCC/MBP-Krab complex and its tight nanomolar affinity make it a good candidate for SAXS. T28_RBCC_R184D was injected onto a Superdex 200 at 4.9 mg/mL, and the T28_RBCC_R184D/MBP-Krab complex was injected at 1:1 and 1:1.5 molar ratios (4.9 mg/mL RBCC with 6.2 or 9.4 mg/mL MBP-Krab) to saturate Krab binding on T28_RBCC [43]. The resulting chromatograms were plotted as *I*(0) *versus* frame number, and the radius of gyration (R_G) across the sample peaks were calculated using CHROMIXS [44]. The R_G remained constant across both sample peaks, indicating that the samples were monodispersed (Fig. 6A). Sample and buffer regions were manually selected for merging and subtraction to generate a buffer corrected scattering curve for each peak. Scattering curves for the complex from both the 1:1 and 1:1.5 molar ratio samples were identical and merged for subsequent analyses. Guinier analysis gave an R_G of 70.1 ± 1.2 Å for T28_RBCC and 63.8 ± 0.5 Å for T28_RBCC/MBP-Krab (Fig. 6B). The paired-distance distribution function of RBCC suggests an elongated dumbbell with a large peak around 40 Å describing the intradomain and cross-sectional distances, and a second peak around 160 Å corresponding to the distance between terminal RING and B-box domains separated by the coiled-coil (Fig. 6C, left). The maximum dimension (Dmax) for the T28_RBCC construct is 232 Å. Upon MBP-Krab binding, the pair-distribution shows an extra peak at 100 Å and a Dmax of 223 Å (Fig. 6C, right).

Scattering curves for T28_RBCC and the T28_RBCC/MBP-Krab complex were then used to generate ab initio bead models in GASBOR [46]. P2 symmetry was imposed for T28_RBCC but not for the T28_RBCC/Krab complex as P2 symmetry could not be supported within a 2:1 complex. The T28_RBCC adopted an elongated dumbbell shape consistent with the expected nature of the antiparallel coiled-coil. Compared with T28_RBCC, the model of the complex shares a similar shape and overall dimension. Extra beads within the complex model are located at the center of the elongated RBCC (Fig. 6D). Taken together, our SAXS analysis shows that MBP-Krab is binding to the central region of TRIM28 RBCC, supporting our model where Krab is binding to the 2-fold symmetry axis on TRIM28 coiled-coil (Fig. 6E).

Site-directed mutagenesis confirms Krab binding to the middle of coiled-coil

To validate our model that Krab is binding to TRIM28's 2-fold symmetry axis, we performed site-directed mutagenesis targeting side-chains found near the 2-fold symmetry axis. The coiled-coil region of TRIM proteins comprises two 30-turn amphipathic helices that run the length of the coiled-coil followed by a hairpin loop that turns toward the center and forms a four-helix bundle [33,34,47,48]. Residues at the coiled-coil dimer interface are highly conserved among TRIM protein members with a leucine (L194 in Rhesus macaque TRIM5α and L306 in Murine TRIM28) found at the two fold symmetry axis being the most conserved residue [34]. We employed the crystal structure of TRIM5α as a homology model to identify the appropriate solvent exposed residues for mutagenesis, while preserving the residues lining the coiled-coil dimer interface (Fig. 7A, Table 2). We designed four "Turn Mutants" (Turns 1 + 2, Turns 3 + 4, Turns 5 + 6, and Turns 7 + 8) that systematically target the central eight turns (V294–N308), as well as four "Face Mutants" (Top Face 2, Top Face 6, Bottom Face 2, and Bottom Face 6), to target residues located on the "Top Face," (away from the four-helix bundle), and opposite "Bottom Face" (involved in four-helix bundle packing) (Fig. 7A). These mutations were cloned into TRIM28 RBCC(58–418) and details of the mutations harboured by each mutant are summarized in Table 2. MBP-Krab pulldown assays were employed to assess the mutants' ability to interact with the Krab domain. The results (Fig. 7B) show that Turns 7 + 8 mutant interacted with ZFP809_Krab similar to the WT. Turns 3 + 4 and 5 + 6 show severely reduced binding. Strikingly, no binding is detected for Turns 1 + 2. The Bottom Face 2 and 6, as well as the Top Face 2 mutant, all showed similar levels of Krab binding compared to WT, whereas the Top Face 6 mutant abolished binding.

Close inspection of the two binding-deficient mutants (Turns 1 + 2 and Top Face 6) reveals that two residues shared between the two mutants, V294 and K297. This prompted us to generate three point mutants, V294E, K297A and K294E, to probe the importance of these two residues. The mutations were cloned into RBCC (58–418)_R184D. Indeed, MBP-Krab pulldown assay demonstrated a complete loss of binding for the K297E mutant, and K297A and V294E both displayed moderate to severe reduction in binding (Fig. 7B). To confirm the K297E mutation blocks binding, we carried out SPR analysis for binding to ZFP932. No binding was detected for RBCC_R184D/K297E even when injected at concentrations up to 75 μM (Fig. 7C). The loss of binding cannot be ascribed to disruption of the overall fold of the RBCC, as SEC-MALLS analysis showed the binding-deficient mutants Turns 1 + 2, Top Face 6 and K297E all share identical elution volumes and M_W with their wild-type counterparts (Supplementary Fig. S7). In conclusion, our mutagenesis data

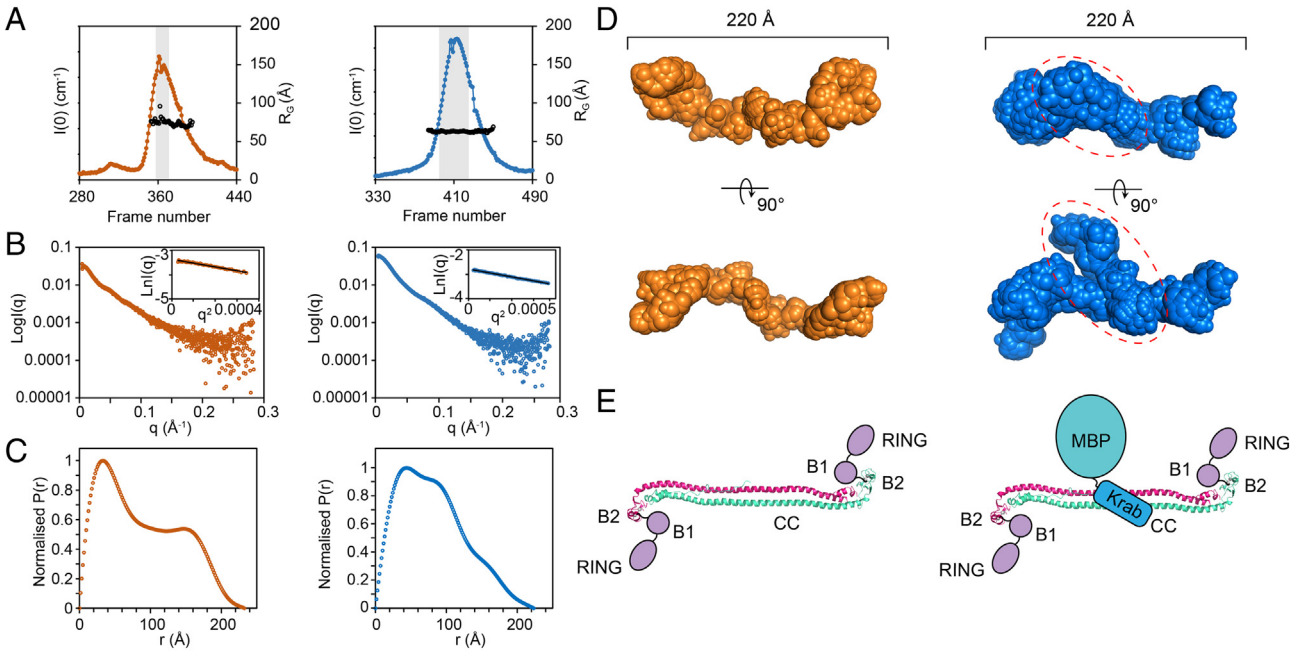

Fig. 6. Solution structure reveal Krab-binding to the center of TRIM28 coiled-coil. SEC-SAXS analysis of RBCC_R184D (orange) and the complex of RBCC_R184D/MBP-Krab-ZFP809 (blue). (A) SEC-SAXS elution profile displaying *I*(0) (joined dots) and R_G (open circles) determined by CHROMIXS [44]. Highlighted gray frames have been used in averaging. (B) Experimental scattering curves of Log*I*(*q*) *versus q*. Insets: enlargement of the Guinier region, displaying good linearity indicating monodispersed samples. (C) Normalized paired-distance distribution functions calculated using GNOM [45]. The maximum dimension (Dmax) for both samples were around 220 Å, consistent with expected values. (D) Solution structure of RBCC_R184D (orange) and the RBCC_R184D/MBP-Krab complex (blue) determined from *ab initio* reconstruction using GASBORI [46]. P2 symmetry has been applied to RBCC_R184D for the reconstruction. The position of MBP-Krab-ZFP809 is indicated with dashed lines and is located on the central region of the elongated RBCC. (E) Models describing the SAXS envelops of RBCC_R184D (left) and RBCC/MBP-Krab (right). The B2-coiled-coil region is represented by the crystal structure of TRIM5α (PDB ID: 4TN3).

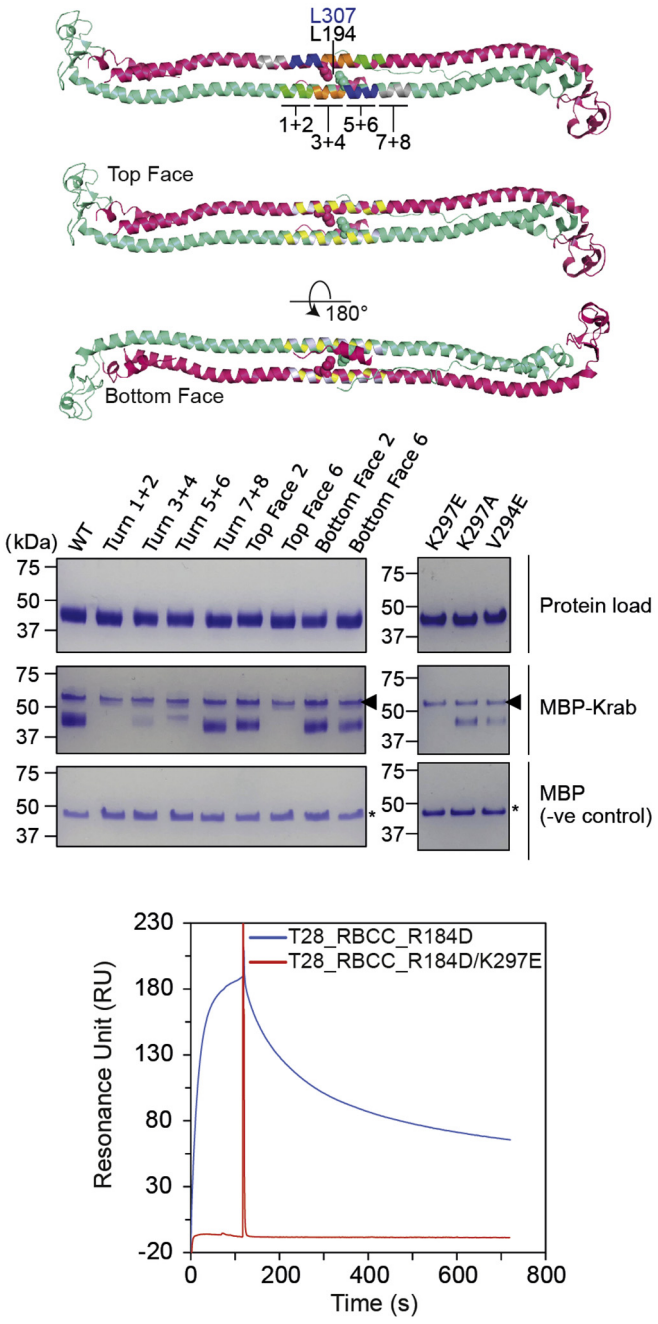

Fig. 7. Site-directed mutagenesis confirms Krab binding the center of TRIM28 coiled-coil. (A) Cartoon representation of TRIM5α's (Rhesus macaque) B-box-coiled-coil crystal structure (PDB ID: 4TN3) with the central leucine L194 (L307 in TRIM28m) shown in spheres. Non-buried residues located on the central 8 α-helical turns have been identified and the equivalent residues in TRIM28 were targeted by mutagenesis (mutants are summarized in Table 2). Four systematic alanine mutants were generated targeting two α-helical turns each: Turn 1 + 2 (green), Turn 3 + 4 (Blue), Turn 5 + 6 (blue) and Turn 7 + 8 (gray). Residues located on the "Top Face" (yellow) and "Bottom Face" (purple) were also targeted by alanine mutations. Two mutants were generated for each face: one mutating the central 2 residues and one spanning a larger 6-residue surface. (B) SDS-PAGE analysis showing the result from MBP-Krab pulldown assay performed on all 11 mutants. Top panels show the purified RBCC mutants used in the experiment, middle panels show their elution profiles with MBP-Krab and bottom panels show the negative control performed with MBP. (C) Biacore SPR experiment confirms K297E mutation abolishes the RBCC/Krab interaction. RBCC_R184D (206 nM) or RBCC_R184D/K297E (75 μM) was flown over the surface of a CAP sensor chip immobilized with biotinylated Krab domain of ZFP932.

validate our model that Krab domain binds to the central region of TRIM28 coiled-coil. The interaction involved the Top Face of the coiled-coil, with K297 being a key residue in binding.

Discussion

Members of the TRIM protein family share a conserved N-terminal domain architecture that has been shown to mediate the formation of both oligomers and key protein–protein interactions. TRIM28 has previously been shown to oligomerize [41], with multiple copies thought to be present at sites of silencing. In this study, we have identified the first Bbox domain (B1) as mediating the formation of higher order oligomers of TRIM28. The structure of this domain identifies a new oligomerization interface on the B1 domain that has not been identified in other Bbox structures, further demonstrating the flexibility of the Bbox as a protein–protein interface.

Although this indicates that multiple copies of TRIM28 may be present at the target locus, mutants disrupting oligomerization show that a single coiled-

Table 2. Summary of residues targeted for mutation in the TRIM28 coiled-coil and the interaction with the Krab domain

Mutant name	Mutations in MuTRIM28	Equivalent residues in RhTRIM5α	Interaction with Krab
Turn 1 + 2	V294A/D295A/K297A/M298A	T181/N182/S184/A185	–
Turn 3 + 4	L301A/Q302A/I303A/K305A	E188/Q189/L190/E192	+
Turn 5 + 6	N308A/K309A/R301A/R312A/V313A/L314A	D195/W196/E197/S199/N200/E201	+
Turn 7 + 8	N316A/D317A/Q319A/K320A/V321A	Q203/N204/E206/K207/E208	+++
Top Face 2	K305A/N308A	E192/D195	+++
Top Face 6	V294A/K297A/L301A/K305A/N308A/R312A	T181/S184/E188/E192/D195/S199	–
Bottom Face 2	E306A/R310A	I193/E197	+++
Bottom Face 6	D295A/A299A/Q302A/E306A/R310A/L314A	N182/D186/Q189/I193/E197/E201	+
K297E	K297E		–
K297A	K297A		++
V294E	V294E		+

The eight central turns of the TRIM28 coiled-coil were targeted for mutagenesis. The TRIM5α coiled-coil domain (PDBid: 4TN3) was used as a template to identify equivalent residues in Murine TRIM28. All residues were then mutated to alanine except for the specific point mutations K297E and V294E. The interaction with the ZFP809 Krab domain was assessed by MBP pulldown.

coil-mediated dimer is sufficient to bind the Krab domain from multiple Krab-ZFPs and can induce effective silencing of a reporter construct in cells. This leads to the obvious question of what role higher-order oligomerization plays in TRIM28 biology. Previous studies have shown that members of the Tif1 subfamily are able to associate to form hetero-oligomers [49–51]. Key interface residues are conserved within family members, suggesting that the B1 domain may act as the interaction interface.

Auto-SUMOylation in the Bromodomain by the PHD finger is a key step in TRIM28-mediated repression as it is required to recruit the downstream chromatin modifiers SETDB1 and the NuRD complex [9,11]. Our *in vitro* SUMOylation assays revealed no significant difference in SUMOylation activity between the wild-type and the B1 assembly-deficient mutants, consistent with our data that B1 assembly is not required for repression in cells. Surprisingly, we observed significant levels of mono- and di-SUMOylation in the T28_RBCCH construct that lacks the PHD/Bromo domain but bears SUMOylation sites K554 and K575. Since the RING domain of members of the TRIM family can act as E3 SUMO ligases [52–54], it is likely that the RING domain is SUMOylating one or both of these sites.

Our investigation of Krab binding demonstrates a clear 2:1 stoichiometry for the interaction between TRIM28 and the Krab domain of Krab-ZFP family members. This is consistent with a single Krab-ZFP protein recognizing a specific genetic locus and recruiting one TRIM28 dimer as a scaffold for downstream events.

Previous reports have suggested that all components of the TRIM28 RBCC are involved in Krab binding [41]. However, it is likely that previous mutations inserted in the RING and Bbox domains have disrupted the overall fold of the TRIM28 protein. In an attempt to generate TRIM28 truncations lacking the N-terminal RING domain, we discovered that the presence of RING domain is essential for the stability of any coiled-coil-containing constructs, as those lacking the RING domain always eluted in the void volume of a Superdex 200 size-exclusion column. We were able to produce a construct consisting of only the second Bbox domain and the coiled-coil region by expressing the intact RBCC with a protease cleavage site inserted between the B1 and B2 domains. This allowed for the removal the N-terminal RING and Bbox domains. This construct bound to the Krab domain in MBP pulldown assays, ruling out the requirement of RING and B1 domains for Krab interaction.

Our mutagenesis data have confirmed our model that a single copy of Krab binds to the center of TRIM28 coiled-coil dimer. The binding site is located on the top face of TRIM28 coiled-coil, and a K297E mutation in this region abolishes the interaction. Interestingly, the K297A mutation only slightly reduced Krab binding, suggesting that the charge of the amino acid side-chain in this position is important. It has been reported that K297 may be a target site for ubiquitylation [55,56] and SUMOylation [57], providing a possible means for regulation of this interaction that warrants further study in the future.

One unresolved question is how the Krab-B box potentiates repression mediated by Krab-A box [24,27]. One possibility is that a Krab-B box may increase the Krab domain's affinity for TRIM28. To probe this hypothesis, we determined the TRIM28 binding affinity for the Krab domains from two members of the Krab A + B class (ZFP809 and Kid3) and one (ZFP932) from the Krab A only class. Unexpectedly, TRIM28 binding affinity achieved by ZFP932 (K_d = 14.7 nM) is comparable to ZFP809 (K_d = 11.7 nM) and around 10-fold higher affinity than Kid3 (K_d = 139.7 nM). Therefore, the Krab-B box does not result in higher affinity for TRIM28, and the mechanism for its auxiliary effect on silencing remains unclear.

Our study provides insights into the initial events during TRIM28-mediated transcription silencing. Our assembly-deficient mutants provide a tool for future studies to understand the specific interactions between the Krab domain and TRIM28 coiled-coil and how this interaction may be regulated during silencing events.

Materials and Methods

Cloning

DNA encoding murine TRIM28 (1–834) was codon optimized and synthesized (GeneArt). The coding sequences for T28_RING (58–139), T28_RB (58–203), T28_B1 (135–203), T28_B2 (200–246), T28_RBCC (58–418), T28_RBCCH (58–597), T28_PB (625–834) and T29_FL (58–834) were amplified by PCR. T28_RING, T28_RB, T28_B2, T28_RBCCH and T28_FL were cloned into pET-47b (+) (N-terminal His-tag) by a ligation-independent cloning (LIC) method [58], while T28_B1 and T28_RBCC were cloned into pET-49b(+)-MBP (N-terminal MBP-His-tag, made in house by replacing the glutathione *S*-transferase tag in pET49b with an MBP tag) using the same LIC method. The resulting constructs contain an N-terminal purification tag followed by a 3-C protease cleavage site to allow tag removal post-affinity purification. The Bbox1 (R184A, R184D, D159K, A181S, A181D, V185D, RV184,185AS) and coiled-coil variants (Supplementary Table S3) were generated by whole plasmid PCR using the wild-type plasmid as template and verified by DNA sequencing. TRIM28-targeted and pFUT-HA-KAP1 lentivectors where assembly mutations were introduced were previously described [16].

The DNA sequence for the Krab domains, ZFP809_Krab (1–74), Kid3_Krab (14–84) and ZFP932_Krab (5–76), were codon optimized and synthesized, subsequently amplified by PCR and cloned into pET-49b(+)-MBP using the same LIC method.

Protein expression and purification

All constructs were expressed in *Escherichia coli* BL21 (DE3) LOBSTR [59] grown in LB media supplemented with 100 μM ZnCl. Expression was induced by the addition of 1 mM IPTG to log phase cultures prior to subsequent growth overnight at 18 °C. Cells were lysed by cell disruption in 20 mM Tris–HCl (pH 8.0), 200 mM NaCl, 0.5 mM Tris(2-carboxyethyl) phosphine (TCEP), 10% (v/v) glycerol and 0.1% (v/v) Triton X-100. The His-tagged TRIM28 constructs were purified using nickel-immobilized metal affinity chromatography, while the MBP-tagged TRIM28 constructs were purified by amylose affinity chromatography. The N-terminal purification tags were removed by cleavage with 3C-protease prior to further purification by anion exchange, and size exclusion chromatography (SEC).

The T28_B2CC construct was expressed and purified as described for His-tagged-RBCC (58–597) with a 3-C protease cleavage site inserted between residues K200 and T201 to allow proteolytic removal of the N-terminal RING and Bbox1 domain (58–200) post-purification. Proteolytic removal of the RING domain after protein purification was necessary to generate non-aggregating coiled-coil containing constructs lacking the RING domain.

The MBP-His-tagged ZFP809_Krab (1–74), Kid3_Krab (14–84) and ZFP932_Krab (5–76) were expressed in *E. coli* as described above. The MBP-Krab fusion proteins were purified using nickel-immobilized metal affinity chromatography to preserve their ability to bind amylose resin in MBP pulldown assays and further purified using anion exchange chromatography.

SEC-MALLS

SEC-MALLS was used to determine the solution molecular weight. Samples (100 μL) were applied to either S75 10/300 GL column [T28m 58–139, 135–203 and variants (except V185D and R184A/V185S variants were applied to an S75 10/300 GL increase column), 200–246, and 625–834] or an S200 Increase 10/300 GL (58–418, 58–597 and 58–834) mounted on a Dionex HPLC equilibrated in 10 mM Tris–HCl, 150 mM NaCl, 3 mM azide and 0.1 mM TCEP (pH 8.0) at a flow rate of 0.5 mL min^{-1}. The scattered light intensity and protein concentration of the column eluate were recorded using a PSS SLD7000 7-angle MALLS detector and a Shodex RI-101 differential refractive index detector (ΔRI) (dn/dc = 0.186), respectively. The weight-averaged molecular mass of material contained in chromatographic peaks was determined from the combined data from both detectors using the PSS winGPC Unichrom software.

Analytical ultracentrifugation

Analytical ultracentrifugation experiments were carried out at 20 °C (293 K) using a Beckman Coulter Model XL-I instrument equipped with an absorbance optical system. Samples (380 μL) and buffer (400 μL) were loaded into double-sector quartz cells and mounted into a Beckman coulter eight-hole An-50 Ti rotor. Prior to the experimental runs, the samples were matched to a buffer containing 10 mM Tris–HCl (pH 8.0) and 150 mM NaCl by extensive dialysis. SEDNTERP [60] was used to calculate a solvent density of 1.00470 g mL^{-1} and viscosity of 0.01002 cp. The protein partial specific volume for T28m 135–203

and 58–203 (0.694 and 0.703 $cm^3\ g^{-1}$, respectively) were calculated from the protein sequence.

SVs of the T28m 135–203 and 58–203 were measured at 50 krpm. Data were analyzed using the *c*(*s*) distributions in SEDFIT [61]. To estimate the half point transition for the monomer–dimer interaction, isotherm analysis of the integrated *c*(*s*) was carried out using the monomer–dimer model in SEDPHAT. Sedimentation equilibrium experiments were carried out at three concentrations for of T28m 135–203 (16, 32, 65 μM) and 58–203 (5, 10, 20 μM), using 110 μL of sample and 120 μL reference and centrifuged at 24,000, 28,000 rpm for 135–203, and 18,000, 22,000 and 26,000 rpm for 58–203. The equilibrium concentration distributions were globally analyzed to ensure that equilibrium had been reached using HeteroAnalysis v1.1.58 [62]. Equilibrium data were collected at a wavelength of 246 and 241 nm for 135–203 and 58–203, respectively, with a step size of 0.001 cm, and averaging of 20 measurements at each step. The data were analyzed using SEDPHAT [63] and a monomer–dimer self-association model was chosen.

Crystallization and structure determination

B1 crystals were grown by vapour diffusion at 18 °C in hanging drops consisting of 1 μL of B1 at 8 mg/mL and 1 μL of reservoir solution (2.7 M ammonium sulfate, pH 6.0). Crystals were harvested and transferred to a drop of cryoprotectant (2.7 M ammonium sulfate, 20% glycerol) prior to being frozen in liquid nitrogen. X-ray diffraction data were collected on Australian Synchrotron beamline MX1 at a wavelength of 0.9537 Å. Data were processed in XDS [64] and AIMLESS [65] (data collection and refinement statistics are presented in Table 1). Experimental phases were determined by single-wavelength anomalous dispersion using the SHELX C/D/E suite [66], and the positions of all four endogenous zinc atoms were identified. Model building and refinement was undertaken in COOT [67] and REFMAC [68], respectively. Model was validated using the program MolProbity [69] before deposited in the PDB with ID 6O5K.

MBP-Krab pulldown assays

Binding assay were carried out with purified recombinant TRIM28 truncations and MBP-Krab fusion proteins (ZFP809 1–74) with an MBP-only negative control. TRIM28 truncations (40–60 μg) were mixed with 20 μg MBP-Krab or MBP, achieving a TRIM28 to MBP-Krab ratio greater than 2:1 to saturate any binding of TRIM28 on MBP-Krab. The mixture was incubated with 50 μL pre-equilibrated amylose resin (NEB) in 450 μL MBP wash buffer [20 mM Tris–HCl (pH 8.0), 200 mM NaCl, 0.5 mM TCEP] and subsequently spun in a 500-μL spin column followed by three washes with MBP wash buffer to remove any unbound proteins. The bound proteins were then eluted with 50 μL MBP elution buffer [20 mM Tris–HCl (pH 8.0), 200 mM NaCl, 0.5 mM TCEP, 20 mM maltose], and the eluted proteins were visualized on a Coommassie-stained SDS-PAGE gel.

In vitro auto-SUMOylation assays

Auto-SUMOylation assays were performed using recombinant proteins produced in *E coli*. E1 (1 μM; SAE1/SAE2), 2 μM E2 UBC9, 10 μM E3 and 50 μM SUMO1 were incubated at 30 °C in the presence of 5 mM ATP for 180 min. Reactions were quenched with SDS-PAGE loading buffer at selected time points, and the SUMOylated species were visualized using SDS-PAGE.

SEC-SAXS

SEC-SAXS data were collected at the Australian Synchrotron SAXS/WAXS beamline at a wavelength of 1.13 Å with a camera length of 3.3 m over a *q*-range of 0.004–0.28 $Å^{-1}$. Samples were extensively dialyzed against 10 mM Tris–HCl (pH 8.0), 300 mM NaCl and 0.1 mM TCEP. Dialyzed samples were injected onto a Superdex 200 increase column and were subjected to SAXS data collection as they eluted. SAXS images were processed using scatterBrain and CHROMIXS [44]. The data were further analyzed using programs in the ATSAS package [70]. *Ab initio* models were produced using GASBOR [46].

Surface plasmon resonance

To generate biotinylated Krab domains, the DNA sequence encoding a specific BirA biotinylation tag GLNDIFEAQKIEWHE (AviTag) was codon optimized and inserted downstream of the 3C protease cleavage site upstream of protein start site using whole plasmid PCR. The AviTagged Krab domains were then co-expressed with pBirA in *E. coli* BL21 (DE3) LOBSTR grown in LB at 37 °C to approximately 0.5 OD_{600}. Cells were then induced with 1 mM IPTG and supplemented with 20 μM D-biotin (Sigma) and grown overnight at 18 °C.

Surface plasmon resonance was performed using a Sensor Chip CAP in a Biacore X100 instrument. CAPture reagent (GE) was loaded onto both the reference and sample surfaces at a flow rate of 5 μL/min for 120 s, achieving a resonance unit (RU) of ~2500. Monobiotinylated Krab domains were then loaded onto the sample surface at 10 μL/min achieving ~50 RU. TRIM28 FL_R184D (400 nM) or RBCC_R184D (206 nM) were flown over the reference and sample surfaces for 120 s, followed by a 600-s wash with SPR buffer [10 mM Tris–HCl (pH 8.0), 300 mM NaCl, 0.1 mM TCEP, 0.005% tween 20]. K_d was determined by fitting a two-state

reaction model using BiacoreX100 Evaluation Software version 2.0.1.

Accession numbers

Coordinates and structure factors have been deposited in the Protein Data Bank with accession number 6O5K. The models and scattering curves for RBCC and the RBCC/MBP-Krab complex were deposited in the SASBDB with ID SASDFS3 and SASDFT3, respectively.

Acknowledgments

This work was supported by a project grant from the Auckland Medical Research Foundation (D.C.G.), a Rutherford Discovery Fellowship from the NZ government administered by the Royal Society of New Zealand (RSNZ) (D.C.G.) and grants from the Swiss National Science Foundation and the European Research Council (ERC 694658) to D.T. Access to analytical ultracentrifuge facilities was funded by the Maurice Wilkins Centre for Molecular Biodiscovery (D. C.G.), a Centre of Research Excellence funded by the NZ government. We acknowledge the New Zealand Synchrotron group for access to the SAXS and MX beam lines at the Australian Synchrotron.

Appendix A. Supplementary data

Supplementary data to this article can be found online at https://doi.org/10.1016/j.jmb.2019.05.002.

Received 8 March 2019;
Received in revised form 29 April 2019;
Available online 9 May 2019

Tripartite motif 28 (TRIM28);
Krüppel-associated box-containing zinc finger proteins (Krab-ZFP);
Endogenous retroviruses (ERVs);
TRIM proteinsPresent address: J.R. Keown, Division of Structural Biology, University of Oxford, Oxford, UK.

Abbreviations used:

ERVs, endogenous retroviruses; ES, embryonic stem; Krab-ZFP, Krüppel-associated box-containing zinc finger protein; SEC-MALLS, size exclusion chromatography coupled to multiangle laser light scattering; SV-AUC, sedimentation velocity analytical ultracentrifuge; SE-AUC, sedimentation equilibrium analytical ultracentrifuge; SEC-SAXS, size exclusion chromatography coupled to small-angle X-ray scattering; LIC, ligation-independent cloning; MBP, maltose binding protein.

References

[1] M. Friedli, D. Trono, The developmental control of transposable elements and the evolution of higher species, Annu. Rev. Cell Dev. Biol. 31 (2015) 429–451.
[2] T. Matsui, D. Leung, H. Miyashita, I.A. Maksakova, H. Miyachi, H. Kimura, et al., Proviral silencing in embryonic stem cells requires the histone methyltransferase ESET, Nature. 464 (7290) (2010) 927.
[3] H.M. Rowe, J. Jakobsson, D. Mesnard, J. Rougemont, S. Reynard, T. Aktas, et al., KAP1 controls endogenous retroviruses in embryonic stem cells, Nature. 463 (7278) (2010) 237–240.
[4] G. Ecco, M. Cassano, A. Kauzlaric, J. Duc, A. Coluccio, S. Offner, et al., Transposable elements and their KRAB-ZFP controllers regulate gene expression in adult tissues, Dev. Cell 36 (6) (2016) 611–623.
[5] D. Esposito, M.G. Koliopoulos, K. Rittinger, Structural determinants of TRIM protein function, Biochem. Soc. Trans. 45 (1) (2017) 183–191.
[6] K. Ozato, D.-M. Shin, T.-H. Chang, H.C. Morse, TRIM family proteins and their emerging roles in innate immunity, Nat. Rev. Immunol. 8 (11) (2008) 849–860.
[7] W.-W. Tsai, Z. Wang, T. Yiu, K. Akdemir, W. Xia, S. Winter, et al., TRIM24 links a noncanonical histone signature to breast cancer, Nature 468 (2010) 927–932.
[8] Q. Xi, Z. Wang, A.-I. Zaromytidou, X.H.F. Zhang, L.-F. Chow-Tsang, J.X. Liu, et al., A poised chromatin platform for TGF-β access to master regulators, Cell. 147 (7) (2011) 1511–1524.
[9] A.V. Ivanov, H. Peng, V. Yurchenko, K.L. Yap, D.G. Negorev, D.C. Schultz, et al., PHD domain-mediated E3 ligase activity directs intramolecular sumoylation of an adjacent bromodomain required for gene silencing, Mol. Cell 28 (5) (2007) 823–837.
[10] L. Zeng, K.L. Yap, A.V. Ivanov, X. Wang, S. Mujtaba, O. Plotnikova, et al., Structural insights into human KAP1 PHD finger-bromodomain and its role in gene silencing, Nat. Struct. Mol. Biol. 15 (6) (2008) 626–633.
[11] X.H. Mascle, D. Germain-Desprez, P. Huynh, P. Estephan, M. Aubry, Sumoylation of the transcriptional intermediary factor 1beta (TIF1beta), the co-repressor of the KRAB multifinger proteins, is required for its transcriptional activity and is modulated by the KRAB domain, J. Biol. Chem. 282 (14) (2007) 10190–10202.
[12] S. Huntley, D.M. Baggott, A.T. Hamilton, M. Tran-Gyamfi, S. Yang, J. Kim, et al., A comprehensive catalog of human KRAB-associated zinc finger genes: insights into the evolutionary history of a large family of transcriptional repressors, Genome Res. 16 (5) (2006) 669–677.
[13] M. Imbeault, P.-Y. Helleboid, D. Trono, KRAB zinc-finger proteins contribute to the evolution of gene regulatory networks, Nature. 543 (7646) (2017) 550–554.
[14] J.H. Thomas, S. Schneider, Coevolution of retroelements and tandem zinc finger genes, Genome Res. 21 (11) (2011) 1800–1812.
[15] F.M. Jacobs, D. Greenberg, N. Nguyen, M. Haeussler, A.D. Ewing, S. Katzman, et al., An evolutionary arms race between KRAB zinc-finger genes ZNF91/93 and SVA/L1 retrotransposons, Nature. 516 (7530) (2014) 242–245.
[16] P. Turelli, N. Castro-Diaz, F. Marzetta, A. Kapopoulou, C. Raclot, J. Duc, et al., Interplay of TRIM28 and DNA methylation in controlling human endogenous retroelements, Genome Res. 24 (8) (2014) 1260–1270.

[17] L. Fasching, A. Kapopoulou, R. Sachdeva, R. Petri, M.E. Jonsson, C. Manne, et al., TRIM28 represses transcription of endogenous retroviruses in neural progenitor cells, Cell Rep. 10 (1) (2015) 20–28.
[18] D. Wolf, S.P. Goff, Embryonic stem cells use ZFP809 to silence retroviral DNAs, Nature. 458 (7242) (2009) 1201–1204.
[19] M. Leseva, B.B. Knowles, D.M. Messerschmidt, D. Solter, Erase-maintain-establish: natural reprogramming of the mammalian epigenome, Cold Spring Harb. Symp. Quant. Biol. 80 (2016) 155–163.
[20] J.R. Friedman, W.J. Fredericks, D.E. Jensen, D.W. Speicher, X.P. Huang, E.G. Neilson, et al., KAP-1, a novel corepressor for the highly conserved KRAB repression domain, Genes Dev. 10 (16) (1996) 2067–2078.
[21] S.S. Kim, Y.M. Chen, E. O'Leary, R. Witzgall, M. Vidal, J.V. Bonventre, A novel member of the RING finger family, KRIP-1, associates with the KRAB-A transcriptional repressor domain of zinc finger proteins, Proc. Natl. Acad. Sci. U. S. A. 93 (26) (1996) 15299–15304.
[22] B. Le Douarin, A.L. Nielsen, J.M. Garnier, H. Ichinose, F. Jeanmougin, R. Losson, et al., A possible involvement of TIF1 alpha and TIF1 beta in the epigenetic control of transcription by nuclear receptors, EMBO J. 15 (23) (1996) 6701–6715.
[23] P. Moosmann, O. Georgiev, B. Le Douarin, J.P. Bourquin, W. Schaffner, Transcriptional repression by RING finger protein TIF1 beta that interacts with the KRAB repressor domain of KOX1, Nucleic Acids Res. 24 (24) (1996) 4859–4867.
[24] H. Vissing, W.K. Meyer, L. Aagaard, N. Tommerup, H.J. Thiesen, Repression of transcriptional activity by heterologous KRAB domains present in zinc finger proteins, FEBS Lett. 369 (2–3) (1995) 153–157.
[25] R. Witzgall, E. O'Leary, A. Leaf, D. Onaldi, J.V. Bonventre, The Kruppel-associated box-A (KRAB-A) domain of zinc finger proteins mediates transcriptional repression, Proc. Natl. Acad. Sci. U. S. A. 91 (10) (1994) 4514–4518.
[26] J.F. Margolin, J.R. Friedman, W.K. Meyer, H. Vissing, H.J. Thiesen, F.J. Rauscher 3rd, Kruppel-associated boxes are potent transcriptional repression domains, Proc. Natl. Acad. Sci. U. S. A. 91 (10) (1994) 4509–4513.
[27] M. Abrink, J.A. Ortiz, C. Mark, C. Sanchez, C. Looman, L. Hellman, et al., Conserved interaction between distinct Kruppel-associated box domains and the transcriptional intermediary factor 1 beta, Proc. Natl. Acad. Sci. U. S. A. 98 (4) (2001) 1422–1426.
[28] N. Born, H.-J. Thiesen, P. Lorenz, The B-subdomain of the *Xenopus laevis* XFIN KRAB-AB domain is responsible for its weaker transcriptional repressor activity compared to human ZNF10/Kox1, PLoS One 9 (2) (2014), e87609.
[29] R. Mannini, V. Rivieccio, S. D'Auria, F. Tanfani, A. Ausili, A. Facchiano, et al., Structure/function of KRAB repression domains: structural properties of KRAB modules inferred from hydrodynamic, circular dichroism, and FTIR spectroscopic analyses, Proteins. 62 (3) (2006) 604–616.
[30] H. Peng, L.C. Gibson, A.D. Capili, K.L. Borden, M.J. Osborne, S.L. Harper, et al., The structurally disordered KRAB repression domain is incorporated into a protease resistant core upon binding to KAP-1-RBCC domain, J. Mol. Biol. 370 (2) (2007) 269–289.
[31] D.C. Schultz, K. Ayyanathan, D. Negorev, G.G. Maul, F.J. Rauscher 3rd, SETDB1: a novel KAP-1-associated histone H3, lysine 9-specific methyltransferase that contributes to HP1-mediated silencing of euchromatic genes by KRAB zinc-finger proteins, Genes Dev. 16 (8) (2002) 919–932.
[32] D.C. Schultz, J.R. Friedman, F.J. Rauscher 3rd, Targeting histone deacetylase complexes via KRAB-zinc finger proteins: the PHD and bromodomains of KAP-1 form a cooperative unit that recruits a novel isoform of the Mi-2alpha subunit of NuRD, Genes Dev. 15 (4) (2001) 428–443.
[33] D.C. Goldstone, P.A. Walker, L.J. Calder, P.J. Coombs, J. Kirkpatrick, N.J. Ball, et al., Structural studies of postentry restriction factors reveal antiparallel dimers that enable avid binding to the HIV-1 capsid lattice, Proc. Natl. Acad. Sci. U. S. A. 111 (26) (2014) 9609–9614.
[34] J.G. Sanchez, K. Okreglicka, V. Chandrasekaran, J.M. Welker, W.I. Sundquist, O. Pornillos, The tripartite motif coiled-coil is an elongated antiparallel hairpin dimer, Proc. Natl. Acad. Sci. U. S. A. 111 (7) (2014) 2494–2499.
[35] D.M. Dawidziak, J.G. Sanchez, J.M. Wagner, B.K. Ganser-Pornillos, O. Pornillos, Structure and catalytic activation of the TRIM23 RING E3 ubiquitin ligase, Proteins. 85 (10) (2017) 1957–1961.
[36] M.G. Koliopoulos, D. Esposito, E. Christodoulou, I.A. Taylor, K. Rittinger, Functional role of TRIM E3 ligase oligomerization and regulation of catalytic activity, EMBO J. 35 (11) (2016) 1204–1218.
[37] J.M. Wagner, M.D. Roganowicz, K. Skorupka, S.L. Alam, D.E. Christensen, G.L. Doss, et al., Mechanism of B-box 2 domain-mediated higher-order assembly of the retroviral restriction factor TRIM5alpha, eLife. 5 (2016).
[38] J.R. Keown, J.X. Yang, J. Douglas, D.C. Goldstone, Characterisation of assembly and ubiquitylation by the RBCC motif of Trim5alpha, Sci. Rep. 6 (2016), 26837.
[39] Z. Yudina, A. Roa, R. Johnson, N. Biris, D.A. de Souza Aranha Vieira, V. Tsiperson, et al., RING dimerization links higher-order assembly of TRIM5alpha to synthesis of K63-linked Polyubiquitin, Cell Rep. 12 (5) (2015) 788–797.
[40] J. Fletcher A., Vaysburd M., Maslen S., Zeng J., Mark Skehel J., J. Towers G., et al. Trivalent RING assembly on retroviral capsids activates TRIM5 Ubiquitination and innate immune signaling. Cell Host Microbe 24:761–775; 2018.
[41] H. Peng, G.E. Begg, D.C. Schultz, J.R. Friedman, D.E. Jensen, D.W. Speicher, et al., Reconstitution of the KRAB–KAP-1 repressor complex: a model system for defining the molecular anatomy of RING-B box-coiled-coil domain-mediated protein-protein interactions, J. Mol. Biol. 295 (5) (2000) 1139–1162.
[42] R.P. Watson, N. Tekki-Kessaris, C.A. Boulter, Characterisation, chromosomal localisation and expression of the mouse Kid3 gene, Biochim. Biophys. Acta 1490 (1–2) (2000) 153–158.
[43] T. Ryan, J.M. Trewhella, J.R. Murphy, J. Keown, L. Casey, F. Grant Pearce, et al., An optimized SEC-SAXS system enabling high X-ray dose for rapid SAXS assessment with correlated UV measurements for biomolecular structure analysis, J. Appl. Crystallogr. 51 (2018) 97–111.
[44] A. Panjkovich, D.I. Svergun, CHROMIXS: automatic and interactive analysis of chromatography-coupled small-angle X-ray scattering data, Bioinformatics. 34 (11) (2017) 1944–1946.
[45] D. Svergun, Determination of the regularization parameter in indirect-transform methods using perceptual criteria, J. Appl. Crystallogr. 25 (4) (1992) 495–503.
[46] D.I. Svergun, M.V. Petoukhov, M.H. Koch, Determination of domain structure of proteins from X-ray solution scattering, Biophys. J. 80 (6) (2001) 2946–2953.
[47] Y. Li, H. Wu, W. Wu, W. Zhuo, W. Liu, Y. Zhang, et al., Structural insights into the TRIM family of ubiquitin E3 ligases, Cell Res. 24 (2014) 762.

[48] C. Weinert, D. Morger, A. Djekic, M.G. Grutter, P.R. Mittl, Crystal structure of TRIM20 C-terminal coiled-coil/B30.2 fragment: implications for the recognition of higher order oligomers, Sci. Rep. 5 (2015), 10819.
[49] H. Peng, I. Feldman, F.J. Rauscher 3rd, Hetero-oligomerization among the TIF family of RBCC/TRIM domain-containing nuclear cofactors: a potential mechanism for regulating the switch between coactivation and corepression, J. Mol. Biol. 320 (3) (2002) 629–644.
[50] B. Herquel, K. Ouararhni, K. Khetchoumian, M. Ignat, M. Teletin, M. Mark, et al., Transcription cofactors TRIM24, TRIM28, and TRIM33 associate to form regulatory complexes that suppress murine hepatocellular carcinoma, Proc. Natl. Acad. Sci. U. S. A. 108 (20) (2011) 8212–8217.
[51] K.W. Fong, J.C. Zhao, B. Song, B. Zheng, J. Yu, TRIM28 protects TRIM24 from SPOP-mediated degradation and promotes prostate cancer progression, Nat. Commun. 9 (1) (2018) 5007.
[52] Q. Liang, H. Deng, X. Li, X. Wu, Q. Tang, T.-H. Chang, et al., TRIM28 is a SUMO E3 ligase and negative regulator of interferon regulatory factor 7, J. Immunol. 187 (9) (2011) 4754–4763.
[53] Y. Chu, X. Yang, SUMO E3 ligase activity of TRIM proteins, Oncogene. 30 (9) (2011) 1108–1116.
[54] P. Wang, S. Benhenda, H. Wu, V. Lallemand-Breitenbach, T. Zhen, F. Jollivet, et al., RING tetramerization is required for nuclear body biogenesis and PML sumoylation, Nat. Commun. 9 (1) (2018) 1277.
[55] N.D. Udeshi, T. Svinkina, P. Mertins, E. Kuhn, D.R. Mani, J. W. Qiao, et al., Refined preparation and use of anti-diglycine remnant (K-epsilon-GG) antibody enables routine quantification of 10,000s of ubiquitination sites in single proteomics experiments, Mol. Cell. Proteomics 12 (3) (2013) 825–831.
[56] V. Akimov, I. Barrio-Hernandez, S.V.F. Hansen, P. Hallenborg, A.-K. Pedersen, D.B. Bekker-Jensen, et al., UbiSite approach for comprehensive mapping of lysine and N-terminal ubiquitination sites, Nat. Struct. Mol. Biol. 25 (7) (2018) 631–640.
[57] I.A. Hendriks, D. Lyon, C. Young, L.J. Jensen, A.C.O. Vertegaal, M.L. Nielsen, Site-specific mapping of the human SUMO proteome reveals co-modification with phosphorylation, Nat. Struct. Mol. Biol. 24 (3) (2017) 325–336.
[58] C. Aslanidis, P.J. de Jong, Ligation-independent cloning of PCR products (LIC-PCR), Nucleic Acids Res. 18 (20) (1990) 6069–6074.
[59] K.R. Andersen, N.C. Leksa, T.U. Schwartz, Optimized *E. coli* expression strain LOBSTR eliminates common contaminants from His-tag purification, Proteins. 81 (11) (2013) 1857–1861.
[60] T.M. Laue, B.D. Shah, T.M. Ridgeway, S.L. Pelletier, Computer-aided interpretation of analytical sedimentation data for proteins, in: S. Harding, A. Rowe, J. Horton (Eds.), Analytical Ultracentrifugation in Biochemistry and Polymer Science, Royal Society of Chemistry, Cambridge 1992, pp. 90–125.
[61] P. Schuck, Size-distribution analysis of macromolecules by sedimentation velocity ultracentrifugation and lamm equation modeling, Biophys. J. 78 (3) (2000) 1606–1619.
[62] J. Cole, J. Lary, HeteroAnalysis, University of Connecticut, Storrs, CT, 2005.
[63] J.C. Houtman, P.H. Brown, B. Bowden, H. Yamaguchi, E. Appella, L.E. Samelson, et al., Studying multisite binary and ternary protein interactions by global analysis of isothermal titration calorimetry data in SEDPHAT: application to adaptor protein complexes in cell signaling, Protein Sci. 16 (1) (2007) 30–42.
[64] W. Kabsch, Integration, scaling, space-group assignment and post-refinement, Acta Crystallogr. Sect. D 66 (2) (2010) 133–144.
[65] P.R. Evans, G.N. Murshudov, How good are my data and what is the resolution? Acta Crystallogr. Sect. D 69 (7) (2013) 1204–1214.
[66] G. Sheldrick, Experimental phasing with SHELXC/D/E: combining chain tracing with density modification, Acta Crystallogr. Sect. D 66 (4) (2010) 479–485.
[67] P. Emsley, B. Lohkamp, W.G. Scott, K. Cowtan, Features and development of Coot, Acta Crystallogr. Sect. D 66 (4) (2010) 486–501.
[68] A.A. Vagin, R.A. Steiner, A.A. Lebedev, L. Potterton, S. Mc Nicholas, F. Long, et al., REFMAC5 dictionary: organization of prior chemical knowledge and guidelines for its use, Acta Crystallogr. Sect. D: Biol. Crystallogr. 60 (Pt 12 Pt 1) (2004) 2184–2195.
[69] V.B. Chen, W.B. Arendall 3rd, J.J. Headd, D.A. Keedy, R.M. Immormino, G.J. Kapral, et al., MolProbity: all-atom structure validation for macromolecular crystallography, Acta Crystallogr. D Biol. Crystallogr. 66 (2010) 12–21 Pt 1.
[70] D. Franke, M.V. Petoukhov, P.V. Konarev, A. Panjkovich, A. Tuukkanen, H.D.T. Mertens, et al., ATSAS 2.8: a comprehensive data analysis suite for small-angle scattering from macromolecular solutions, J. Appl. Crystallogr. 50 (2017) 1212–1225 Pt 4.